

Grid-Forming Hybrid Angle Control: Behavior, Stability, Variants and Verification

Ali Tayyebi, Denis Vettoretti, Adolfo Anta, and Florian Dörfler

Abstract—This work explores the stability, behavior, variants, and a controller-hardware-in-the-loop (C-HiL) verification of the recently proposed grid-forming (GFM) hybrid angle control (HAC). We revisit the foundation of GFM HAC, and highlight its behavioral properties in relation to the conventional synchronous machine (SM). Next, we introduce the required complementary controls to be combined with the HAC to realize a GFM behavior. The characterization of the analytical operating point and nonlinear energy-based stability analysis of a grid-connected converter under the HAC is presented. Further, we consider various output filter configurations and derive an approximation for the original control proposal. Moreover, we provide details on the integration of GFM HAC into a complex converter control architecture and introduce several variants of the standard HAC. Finally, the performance of GFM HAC is verified by several test scenarios in a C-HiL setup to test its behavior against real-world effect such as noise and delays.

Index Terms—grid-forming control, hybrid angle control, controller-hardware-in-the-loop, grid-connected converter.

I. INTRODUCTION

The global shift toward the massive integration of energy generation from renewable source accompanied by the supply chain concerns associated with conventional energy generation has raised significant interest in converter-based systems. Thus, power converters are perceived as the vital corner stones of the modern power system and are expected to replace the well-established SM technology. However, a robust and reliable control of power converters in a converter-dominated power system is to some extent an open question. The emerging grid-forming (GFM) control synthesis in contrast to the classic grid-following (GFL) converter control concept is envisioned to address the stability challenges in a converter-dominated power grid [1]–[7]. On the other hand, it is worth mentioning that the power system operators are actively designing test procedures and grid code requirements for the GFM converters, as well, e.g., [8], [9].

The broadly recognized droop control serves as a powerful baseline GFM control candidate that mimics the behavior of a SM governor for the power converters [10]–[12]. As the natural extension of the droop control, the virtual synchronous machine concept is proposed that emulates the SM dynamics (up to different degrees of accuracy) [13], [14]. On the other hand, the matching-type GFM controllers are

proposed that synthesize the converter control based on the structural dynamic similarities with the SM [15], [16]. Along a different design direction, the nonlinear oscillators dynamics are recently exploited for a GFM control design [17]–[19]. Finally, the combination of aforementioned techniques has resulted in several hybrid control architectures [20]–[23].

The GFM HAC relies on a combination of the dc matching control and ac synchronization term that resembles the droop control and/or Kuramoto oscillator dynamics [24]. The theoretic control design and system-level simulation-based performance investigation of the HAC are previously explored [20], [25]–[27]. Previous works highlight 1) the strong stability properties of the HAC under mild parametric conditions, 2) system-level frequency stability enhancement, 3) stabilizing behavior in complex hybrid ac/dc power grids, and finally, 4) robustness with respect to (w.r.t.) the nonlinear phenomena such as current limitation and grid split.

In this paper, we highlight further details on the behavioral properties of the GFM HAC, provide a closed-form characterization of the converter operating point, formulate an intuitive energy-based stability analysis, provide an approximate form of the HAC, and disclose several variants of the standard HAC. Last but not least, the performance of GFM HAC is verified by several test scenarios in a C-HiL setup that utilizes an OPAL-RT simulator and external control cards.

The remainder of this paper is structured as it follows. Section II describes the dynamic modeling of a grid-connected converter, introduces the HAC, and discusses its behavioral properties. Section III presents the closed-loop analysis. Section IV provides details on the weak grid connection, HAC approximation, and its variants. Section V provides C-HiL performance verification, and Section VI concludes the paper.

II. CONVERTER CONNECTED TO A STIFF GRID

In this section, we present the dynamic modeling of a grid-connected converter, revisit the GFM HAC strategy, and discuss its behavioral properties.

A. Physical converter system dynamics

Let us consider a two-level dc-ac power converter model that is interfaced to a stiff grid (i.e., with constant frequency and voltage magnitude) through a resistive-inductive element [15]; see Figure 1. The open-loop dc voltage and ac current dynamics of such system are described by

$$C_{dc} \frac{dv_{dc}}{dt} = i_{dc} - G_{dc} v_{dc} - i_s, \quad (1a)$$

$$L \frac{di_{abc}}{dt} = v_{s,abc} - R i_{abc} - v_{g,abc}, \quad (1b)$$

A. Tayyebi (the corresponding author) is with the Hitachi Energy Research (HER), 72226 Västerås, Sweden, and Automatic Control Laboratory, ETH Zürich, 8092 Zürich, Switzerland, e-mail: ali.tayyebi@hitachienergy.com, D. Vettoretti and A. Anta are with the Austrian Institute of Technology (AIT), 1210 Vienna, Austria and F. Dörfler is with the Automatic Control Laboratory, ETH Zürich, 8092 Zürich, Switzerland. This work was funded in parts by the HER, AIT, and ETH funds.

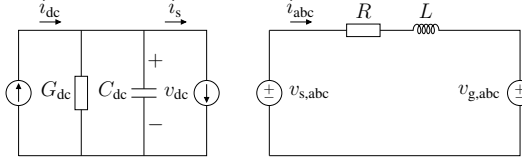


Fig. 1. The circuit diagram associated with the open-loop dynamics of the grid-connected converter model as in (1).

where C_{dc} denotes the dc-link capacitance, v_{dc} denotes the dc-link voltage, i_{dc} denotes the current flowing out of the dc energy source, G_{dc} denotes the dc conductance that models the dc-side losses, and i_s denotes the dc-side switched current. Further, L denotes the ac-side inductance that models the converter output filter, i_{abc} denotes the converter output current flowing into the grid, $v_{s,abc}$ denotes the ac-side switched voltage, R denotes the equivalent series resistance of the filter inductance, and finally $v_{g,abc}$ denotes the balanced voltage of the stiff ac grid at nominal frequency ω_0 and magnitude v_0 .

B. Energy source model and control

The dc current source in Figure 1 that models the primary dc energy source e.g., a battery, can be controlled in several ways. One can close the loop by considering a proportional controller to increase the dc voltage damping [5]. Further, it is possible to also include integral and derivative terms to enhance the dc voltage reference tracking and dynamic performance. Thus, the i_{dc} in (1a) takes generic form

$$i_{dc} = -\kappa_p (v_{dc} - v_{dc,r}) - \kappa_i \int_0^t (v_{dc} - v_{dc,r}) d\tau - \kappa_d \frac{dv_{dc}}{dt}, \quad (2)$$

where κ_p , κ_i , and κ_d denote the parameters of the proportional-integral-derivative control. Note that one can implement the derivative term in (2) by measuring the dc-link capacitance current (since they are equivalent up to a constant factor). Previous work investigated the contribution of control (2) to the frequency damping and inertial response under the GFM matching control [15], [28]. Finally, if the energy source is not controllable, e.g., battery-integrated system without a dc-dc converter stage, one can fix i_{dc} to a constant reference.

C. Power-preserving averaged dc-ac converter model

The dc-ac converter (1) is represented by the switched current and voltage pair $(i_s, v_{s,abc})$. Let us introduce the balanced three-phase converter modulation signal

$$m_{abc} = \mu \left[\cos \theta, \cos \left(\theta + \frac{2\pi}{3} \right), \cos \left(\theta - \frac{2\pi}{3} \right) \right]^\top, \quad (3)$$

where μ and θ respectively denote the modulation signal magnitude and phase angle. Next, the lossless power-preserving averaged model of the two-level converter is given by [29]

$$i_s = m_{abc}^\top i_{abc}, \quad (4a)$$

$$v_{s,abc} = v_{dc} m_{abc}. \quad (4b)$$

In the sequel, we show how μ and θ are selected. Aside from the nonlinear power-preserving model (4), other approaches can be considered.

- One can assume decoupled dc and ac dynamics that is usually verified by considering a sufficiently fast dc voltage control [10], [13], [14]. In this viewpoint, the converter is seen as an ideal controllable voltage source.
- Another trend is to model the internal dynamics of the dc-ac converters by oscillator dynamics. This approach is often adopted when studying the stability of interconnected converter-based systems; see [17] for a review and [12], [18] for experimental investigations.
- Recent works highlight the application of hybrid systems theory in modeling the converter dynamics. These works consider a blend of discontinuous and continuous signals in converter dynamical description, therefore, do not distinguish between the switching and continuous averaged converter models; e.g., see [30], [31].

D. Grid-forming hybrid angle control strategy

In this subsection, we briefly revisit the design of grid-forming HAC [20], [25]–[27]. Let us begin by defining the converter relative angle w.r.t. the grid model in Figure 1. The modulation angle θ in (3) enters $v_{s,abc}$ in (4) that subsequently appears in (1b) (as the voltage behind output filter). Let us define ω as the converter angular frequency that is given by the time-derivative of θ . Similarly, let θ_g and ω_g respectively denote the phase angle and the angular frequency grid voltage $v_{g,abc}$ in (1b) and Figure 1. Note that $\omega_g = \omega_0$, since we consider a stiff grid. Thus, the converter-grid relative angle and its derivative are given by

$$\delta = \theta - \theta_g, \quad (5a)$$

$$\frac{d\delta}{dt} = \frac{d\theta}{dt} - \frac{d\theta_g}{dt} = \omega - \omega_g = \omega - \omega_0. \quad (5b)$$

The GFM HAC that defines the converter frequency (hence the modulation angle) takes the form

$$\omega = \omega_0 + \underbrace{\kappa_{dc} (v_{dc} - v_{dc,r})}_{\text{dc matching term}} - \underbrace{\kappa_{ac} \sin \left(\frac{\delta - \delta_r}{2} \right)}_{\text{ac synchronization term}}, \quad (6)$$

where $v_{dc,r}$ and δ_r respectively denote the dc voltage and relative angle references. It is worth mentioning that the dc part of (6) is similar to the matching control [15], [16], [32]. On the other hand, the ac part of the HAC realizes the frequency synchronization via nonlinear angle damping assignment. The prior works [5], [20], [27] provide detailed discussions on the properties of GFM controls that depend on the ac and/or dc quantities. Nonetheless, in a nutshell, incorporating the dc feedback in the frequency dynamics tends to enhance the robustness and including the ac feedback enhances the dynamic performance; see [21], [27], [33], [34] for theoretic and numerical investigations. The HAC (6), while defining the converter frequency, behaves as a synchronization mechanism. To further elaborate, if the converter dc voltage is sufficiently

regulated, i.e., $v_{dc} \approx v_{dc,r}$, then the converter-grid relative angle dynamics (5b) reduces to

$$\frac{d\delta}{dt} \approx -\kappa_{ac} \sin\left(\frac{\delta - \delta_r}{2}\right). \quad (7)$$

This means if $\delta > \delta_r \Rightarrow d\delta/dt < 0 \Rightarrow \delta \downarrow$ and similarly, if $\delta < \delta_r \Rightarrow d\delta/dt > 0 \Rightarrow \delta \uparrow$. The HAC potentially replaces the synchronization mechanism (e.g., phase-locked loop, virtual synchronous machine, active power control sub-systems) in converter control architectures; see Figure 5. For instance, HAC is a synchronizing control candidate for the

- high voltage direct current (HVDC) converters in embedded, inter-connector, multi-terminal, and offshore wind farm integration setups,
- flexible ac transmission system (FACTS) devices,
- low-voltage photovoltaic (PV) and battery systems,
- and, utility-scale battery energy storage system (BESS).

E. DC voltage and AC power flow regulation

The HAC regulates the dc voltage and ac power flow through frequency synchronization. To further elaborate, let us consider two separate cases.

1) *Pure dc feedback control*: assume $\kappa_{dc} \neq 0$ and $\kappa_{ac} = 0$ that reduces (6) to

$$\Delta\omega = \omega - \omega_0 = \kappa_{dc} (v_{dc} - v_{dc,r}) = \kappa_{dc} \Delta v_{dc}. \quad (8)$$

This controller combination is the reduction of HAC to the matching control [15]. It is established that under the matching control, i.e., when the converter frequency is defined proportional to the dc voltage, the converter dynamics are structurally similar to that of the SM. Therefore, the converter exhibits self-synchronizing behavior of the SM [16] which means

$$\omega \rightarrow \omega_0 \Rightarrow \Delta\omega \rightarrow 0 \Rightarrow \Delta v_{dc} \rightarrow 0 \Rightarrow v_{dc} \rightarrow v_{dc,r}.$$

Thus, the frequency synchronization implies dc voltage regulation, that is achieved by modifying the ac power. This control mode is particularly interesting in weak dc-link applications.

2) *Pure ac feedback control*: consider the gain combination $\kappa_{dc} = 0$ and $\kappa_{ac} \neq 0$. Let us approximate the ac term in (6) with the ac power flow deviation, i.e., assume that $\Delta\delta = \delta - \delta_r$ is proportional to $\Delta p = p - p_r$ up to a constant factor $\kappa_{\delta-p}$. Then, (6) reduces to

$$\Delta\omega \approx -\kappa_{ac} \sin\left(\frac{\kappa_{\delta-p} \Delta p}{2}\right) \approx -\left(\frac{\kappa_{ac} \kappa_{\delta-p}}{2}\right) \Delta p, \quad (9)$$

assuming that Δp is sufficiently small. This variant represents the power-frequency droop control embedded in HAC, thus,

$$\omega \rightarrow \omega_0 \Rightarrow \Delta\omega \rightarrow 0 \Rightarrow \Delta p \rightarrow 0 \Rightarrow p \rightarrow p_r.$$

In this case, frequency synchronization implies ac power flow regulation, that is achieved by the power injection/absorption of the dc-link. This control mode is particularly interesting in stiff dc-link applications. Finally, the hybrid configuration under appropriate tuning provides seamless transition between the aforementioned modes [20], [22].

F. Behavioral interpretations and connections to the SM

It is possible to interpret the structure of HAC in relation to SM control and behavior. Firstly, the influence of a governor on the SM behavior is perceived as modifying the turbine output mechanical power p_m according to the mechanical frequency ω_m deviation from its reference $\omega_{m,r}$. In other words,

$$p_m = p_{m,r} - \kappa_{\omega-p} (\omega_m - \omega_{m,r}), \quad (10)$$

where $p_{m,r}$ and $\kappa_{\omega-p}$ respectively denote the turbine reference power and governor control gain. Observe that if $\omega_m \uparrow \downarrow \Rightarrow p_m \downarrow \uparrow$ to accordingly modify the energy input into the SM such that the frequency is stabilized. One can alternatively rewrite (10) as the so-called droop control, i.e.,

$$\omega_m = \omega_{m,r} - \frac{1}{\kappa_{\omega-p}} (p_m - p_{m,r}). \quad (11)$$

Now, under the small power-angle assumption, i.e., $\Delta\delta \propto \Delta p$ one can interpret the ac part of the HAC (6) as droop control (9) which takes the same form as (11). Therefore, the ac term in (6) mimics the stabilizing influence of the turbine governor.

Next, let us revisit the modeling of SM inertial response [35]. We assume that the mechanical power p_m is flowing into the SM and electrical power p_e is flowing out of its ac terminal. These two quantities are linked through the time-derivative of kinetic energy E_k stored in the SM rotor, i.e.,

$$\frac{dE_k}{dt} = p_m - p_e \quad \text{where} \quad E_k = \frac{1}{2} J \omega^2 \quad (12)$$

and J denotes the rotor moment of inertia. A salient feature of the SM is that if there is an imbalance between its mechanical and electrical powers, e.g., due to load variation, the rotating mass acts as an energy buffer and provides/absorbs the excess power to restore the power balance. The resulting influence is the SM frequency variation, i.e.,

$$\text{if } \frac{dE_k}{dt} = J\omega \frac{d\omega}{dt} > 0 \text{ (or } < 0) \Rightarrow \omega \uparrow (\downarrow). \quad (13)$$

The dc-ac power converters, by design, incorporate a similar mechanism. To further elaborate, let p_{dc} denote the power that is flown into the converter dc-link and p_{ac} is the power that is flown out of the converter ac terminal. These quantities are linked together through the potential energy E_p that is stored in the converter dc-link, i.e.,

$$\frac{dE_p}{dt} = p_{dc} - p_{ac} \quad \text{where} \quad E_p = \frac{1}{2} C_{dc} v_{dc}^2. \quad (14)$$

Similarly, the power imbalance between the converter dc and ac ports is compensated by the dc-link energy variation, i.e.,

$$\text{if } \frac{dE_p}{dt} = C_{dc} v_{dc} \frac{dv_{dc}}{dt} > 0 \text{ (or } < 0) \Rightarrow v_{dc} \uparrow (\downarrow). \quad (15)$$

From this perspective, the dc term in HAC (6) that relates the converter frequency to the dc voltage (i.e., $\omega \propto v_{dc}$), resembles the inertial response of the SM and links the converter frequency to the available physical stored energy in the dc-link capacitance.

G. AC voltage control

The GFM HAC is primarily designed as an active power-frequency controller [20]. Thus, one has to consider complementary ac voltage control. Similar to other grid-forming controls [5], there are different control candidates.

- One can implement a proportional-integral (PI) (or simply a proportional) ac voltage control that processes the point of common coupling (PCC) voltage error and provides a reference magnitude for converter modulation in (3) [27].
- Another alternative is to define the modulation signal magnitude based on a reactive power and voltage droop control [6], [7]. In this approach, the converter modulation magnitude is modified if the reactive power deviates from its reference. Thus, the modulation magnitude modification indirectly controls the PCC voltage.
- The most straightforward, although less robust, approach is to define the reference magnitude for the converter modulation signal according to the desired references for the dc and ac voltages [20].

H. Control implementation and filtering requirement

The previous work [27], establish that HAC (6) can be exactly constructed based on the dc voltage measurement, internal converter modulation angle, and the grid voltage measurement in Figure 1. To recapitulate, one should firstly expand the ac term in (6), i.e.,

$$\sin\left(\frac{\delta - \delta_r}{2}\right) = \sin\frac{\delta}{2}\cos\frac{\delta_r}{2} - \cos\frac{\delta}{2}\sin\frac{\delta_r}{2}. \quad (16)$$

Then, the terms depending on δ_r can be computed according to the prescribed power and voltage set-points [20]. Next, the terms depending on $\delta = \theta - \theta_g$ are constructed based on the sines and cosines of θ and θ_g that can be respectively obtained from the converter modulation signal m_{abc} and the grid voltage $v_{g,abc}$. Note that it is standard practice to low-pass filter the dc voltage feedback in (6) and the grid voltage measurement to remove the potential dc ripple and ac noise, respectively.

III. CLOSED-LOOP STABILITY ANALYSIS

In what follows, we select a combination of the controls described in the previous section, construct the closed-loop dynamics, and investigate the overall system stability.

A. Closed-loop system formulation

Let us begin by transforming the three-phase dynamics (1) to the stationary $\alpha\beta$ -coordinates by using the standard Clarke transformation [29] that results in

$$C_{dc} \frac{dv_{dc}}{dt} = i_{dc} - G_{dc}v_{dc} - i_s, \quad (17a)$$

$$L \frac{di_{\alpha\beta}}{dt} = v_{s,\alpha\beta} - Ri_{\alpha\beta} - v_{g,\alpha\beta}. \quad (17b)$$

Next, we select the PI dc voltage control¹ (for an enhanced dynamic performance and robustness) from (2), i.e.,

$$\begin{aligned} \frac{d\zeta}{dt} &= v_{dc} - v_{dc,r}, \\ i_{dc} &= -\kappa_p(v_{dc} - v_{dc,r}) - \kappa_i\zeta, \end{aligned}$$

where ζ denotes the integrator state, the HAC (6), and the feedforward ac voltage control, i.e.,

$$\mu = \frac{v_r}{v_{dc,r}}. \quad (19)$$

Therefore, all three control inputs, i.e., the dc energy source current, modulation magnitude, and angle are well-defined (the latter is obtained by integrating the converter frequency defined by (6)). Next, we consider rotating dq-coordinates [29] that are aligned with the grid angle θ_g , thus, rotating with the grid frequency ω_g . The closed-loop dynamics in rotating dq-coordinates is represented by

$$\frac{d\delta}{dt} = \kappa_{dc}(v_{dc} - v_{dc,r}) - \kappa_{ac} \sin\left(\frac{\delta - \delta_r}{2}\right), \quad (20a)$$

$$\frac{d\zeta}{dt} = v_{dc} - v_{dc,r}, \quad (20b)$$

$$\begin{aligned} C_{dc} \frac{dv_{dc}}{dt} &= -\kappa_p(v_{dc} - v_{dc,r}) - \kappa_i\zeta - G_{dc}v_{dc} \\ &\quad - \mu(i_d \cos \delta + i_q \sin \delta), \end{aligned} \quad (20c)$$

$$L \frac{di_d}{dt} = \mu v_{dc} \cos \delta - Ri_d - L\omega_0 i_q - v_{g,d}, \quad (20d)$$

$$L \frac{di_q}{dt} = \mu v_{dc} \sin \delta - Ri_q + L\omega_0 i_d. \quad (20e)$$

We remark that $v_{g,d} = v_0$ (i.e., the nominal voltage magnitude of the stiff grid) and $v_{g,q} = 0$ since the d-axis is aligned with θ_g . Moreover, it is important to emphasize that the closed-loop system is nonlinear due to HAC in (20a) and modulated trigonometric terms in (20c) and (20d).

B. Analytical derivation of equilibria

In order to evaluate the stationary operating points (denoted by star superscript) of the closed-loop system, we begin by setting the right-hand side (RHS) of the (20) to zero, i.e.,

$$\kappa_{dc}(v_{dc}^* - v_{dc,r}) - \kappa_{ac} \sin\left(\frac{\delta^* - \delta_r}{2}\right) = 0, \quad (21a)$$

$$v_{dc}^* - v_{dc,r} = 0, \quad (21b)$$

$$\begin{aligned} -\kappa_p(v_{dc}^* - v_{dc,r}) - \kappa_i\zeta^* - G_{dc}v_{dc}^* \\ - \mu(i_d^* \cos \delta^* + i_q^* \sin \delta^*) = 0, \end{aligned} \quad (21c)$$

$$\mu v_{dc}^* \cos \delta^* - Ri_d^* - L\omega_0 i_q^* - v_{g,d} = 0, \quad (21d)$$

$$\mu v_{dc}^* \sin \delta^* - Ri_q^* + L\omega_0 i_d^* = 0. \quad (21e)$$

Hence, one can solve (21a) and (21b) to evaluate δ^* and v_{dc}^* . Next, it is possible to solve (21d) and (21e) that result in the closed-form expressions for i_d^* and i_q^* that are the functions

¹The previous works on HAC [20], [25]–[27] do not include the integral term in their dc voltage controls, therefore, the forthcoming closed-loop system analysis (although conceptually similar) differs from the prior investigations. In particular, the PI dc voltage control consideration omits the previously required assumption to prove the existence and derive a closed-form expression of the closed-loop stationary operating points.

$$\begin{aligned} \frac{dV(\hat{x})}{dt} &= \left(\frac{c_1}{2} \sin \frac{\hat{\delta}}{2} \right) \frac{d\hat{\delta}}{dt} + 2 \left(\left(c_2 \hat{\zeta} \right) \frac{d\hat{\zeta}}{dt} + (c_3 \hat{v}_{dc}) \frac{d\hat{v}_{dc}}{dt} + (c_4 \hat{i}_d) \frac{d\hat{i}_d}{dt} + (c_5 \hat{i}_q) \frac{d\hat{i}_q}{dt} \right), \\ &= \left(\frac{c_1}{2} \sin \frac{\delta - \delta^*}{2} \right) \frac{d\delta}{dt} + 2 \left(c_2 (\zeta - \zeta^*) \frac{d\zeta}{dt} + c_3 (v_{dc} - v_{dc}^*) \frac{dv_{dc}}{dt} + c_4 (i_d - i_d^*) \frac{di_d}{dt} + c_5 (i_q - i_q^*) \frac{di_q}{dt} \right). \end{aligned} \quad (25)$$

of δ^* and v_{dc}^* . Finally, one can solve (21c) to find ζ^* . Thus, (letting $k \in \{1, 2\}$) the steady-state system of equations (21) yields the following operating points,

$$\delta^* = \delta_r + 2\pi k, \quad (22a)$$

$$v_{dc}^* = v_{dc,r}, \quad (22b)$$

$$\zeta^* = \frac{-G_{dc} v_{dc}^* - \mu (i_d^* \cos \delta^* - i_q^* \sin \delta^*)}{\kappa_i}, \quad (22c)$$

$$i_d^* = \frac{\mu v_{dc}^* (R \cos \delta^* - L\omega_0 \sin \delta^*) - R v_{g,d}}{R^2 + (L\omega_0)^2}, \quad (22d)$$

$$i_q^* = \frac{\mu v_{dc}^* (L\omega_0 \cos \delta^* + R \sin \delta^*) - L\omega_0 v_{g,d}}{R^2 + (L\omega_0)^2}. \quad (22e)$$

We remark that due to the periodicity of (22c)-(22e) w.r.t. δ , the steady-state quantities ζ^* , i_d^* , and i_q^* are identical for either δ_r or $\delta_r + 2\pi$ [20]. In the next subsection, we investigate the stability of the operating point in (22) that is characterized by $\delta^* = \delta_r$, i.e.,

$$x^* = (\delta_r, \zeta^*, v_{dc}^*, i_d^*, i_q^*). \quad (23)$$

In the sequel, we restrict our focus to a local state space region around the stationary point (23) that excludes the other angle equilibrium in (22a). The reader is referred to [20] for a global (i.e., large-signal) stability analysis².

C. Nonlinear energy-based stability analysis

The system (20) is characterized by the nonlinearities due to the HAC in (20a), and the modulated current and voltage terms in (20c)-(20e). One potential approach to analyze the stability of the operating point (23), is to linearize the (20) and investigate the eigenvalues of resulting linear system. However, due to the particular structure of the Jacobian associated with (20), it is not straightforward to derive the analytical closed-form expressions for the eigenvalues evaluated at (23).

A more comprehensive nonlinear analysis approach is to associate a so-called *energy function* with the closed-loop dynamics (20) and study the behavior of this function w.r.t. the evolution of states in (20). The energy function behavior (under certain conditions) reveals the stability properties of the system. More precisely, let us define an energy function

$$V(\hat{x}) = c_1 \left(1 - \cos \frac{\hat{\delta}}{2} \right) + c_2 \hat{\zeta}^2 + c_3 \hat{v}_{dc}^2 + c_4 \hat{i}_d^2 + c_5 \hat{i}_q^2, \quad (24)$$

where $\hat{x} = x - x^*$, $\hat{\delta} = \delta - \delta^*$, $\hat{\zeta} = \zeta - \zeta^*$, $\hat{v}_{dc} = v_{dc} - v_{dc}^*$, $\hat{i}_d = i_d - i_d^*$, and $\hat{i}_q = i_q - i_q^*$ and all the coefficients in (24) are positive constants. Let us consider the derivative of (24)

w.r.t. time as in (25). The state-dependent function (24) can be perceived as a measure of the distance (i.e., error) between the states in (20) and the equilibrium point (23).

Given that $V(0) = 0$ and $V(\hat{x}) > 0$ for $x \neq x^*$, we can conclude that $V(\hat{x}) \rightarrow 0$ (thus, $\hat{x} \rightarrow 0$ and $x \rightarrow x^*$) if $dV(\hat{x})/dt < 0$ for all $x \neq x^*$ (i.e., if $V(\hat{x})$ is strictly decreasing). Hence, the convergence of $V(\hat{x})$ to zero implies the stability of (20). In order to demonstrate the stability of system (20), we seek for a parametric condition that results in $dV(\hat{x})/dt < 0$ for all $x \neq x^*$. Following the procedure in [20, Theorem 2], we set the coefficients in (24) as

$$c_1 = \frac{4}{\kappa_{dc}}, c_2 = \frac{\kappa_i}{2}, c_3 = \frac{C_{dc}}{2}, \text{ and } c_4 = c_5 = \frac{L}{2}.$$

Subsequently, lengthy albeit straightforward computation as in [20, Theorem 2] [36] shows that if

$$\rho = \frac{\kappa_{ac}}{\kappa_{dc}} > \rho_{\text{critical}}, \quad (26)$$

where

$$\rho_{\text{critical}} = \frac{1}{G_{dc} + \kappa_p} + \frac{\mu^2 (i_d^{*2} + i_q^{*2})}{G_{dc} + \kappa_p} + \frac{\mu^2 v_{dc}^{*2}}{R},$$

then $dV(\hat{x})/dt < 0$. We remark that the condition (26) is met by choosing a sufficiently large ac synchronization gain in (6). Note that the implication of the stability condition (26) is the fact that the closed-loop stability is guaranteed solely by an appropriate choice of the HAC ac and dc gains. Further, ρ_{critical} can be reduced by increasing the proportional gain of the dc voltage control, thus, allowing for a less aggressive tuning of the HAC; see [20] for details on the stability condition (26). Last, Figure 2 provides a conceptual example for the presented energy-based stability analysis where a simplified form of (24) is employed. Figure 2 shows that how different initial states converge to the desired equilibrium point if the energy decay, i.e., $dV(\hat{x})/dt < 0$ is guaranteed.

IV. CONVERTER CONNECTED TO A WEAK GRID

In this section, we consider more complex model configurations in contrast to the model presented in Figure 1. Further, an approximate variant of HAC is presented. Next, we show how HAC can be combined with classic cascaded current and voltage controls. Finally, we present several HAC variants.

A. Grid impedance consideration

A weak grid connection is considered by including an equivalent grid impedance that is represented by a resistive-inductive element as shown in Figure 3. The different ratios of L_g and R_g represent connection to the low, medium, and high voltage grids [6]. Since the serial connected filter and

²We remark that the forthcoming analysis can be extended to provide large-signal, i.e., global stability guarantees, as well. However, in this paper, for the sake of brevity, a local analysis is provided.

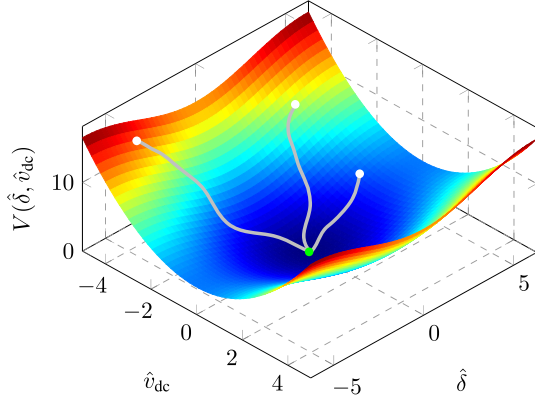


Fig. 2. Conceptual illustration of the energy-based stability analysis; here it is assumed that the energy function is only function of the relative angle and dc voltage, i.e., $V(\delta, \hat{v}_{dc}) = 2(1 - \cos \delta/2) + (1/2)\hat{v}_{dc}^2$.

grid equivalent impedances can be merged together, the closed-loop dynamics associated with the model in Figure 3 takes the same form as in (20). The main implication of a weak grid connection is the fact that $v_{g,abc}$ (in Figure 1) is not available for the control implementation; see subsection II-H and [20]. Next, we show how leveraging certain assumptions allows to counteract this limitation by deriving an approximation for the HAC based on the ac active power flow.

B. Power-based control approximation

Consider the model in Figure 3 and let us merge the filter and grid equivalent impedance into a unified resistive-inductive element that reduces the ac sub-circuit to a classic coupled voltage sources configuration as in [6, Figure 7]. Subsequently, under dominantly inductive grid and small power angle assumptions [6], [11], the relative angle between $v_{s,abc}$ and $v_{g,abc}$ is linearly approximated by the active power flows, i.e.,

$$\delta \approx \sin(\delta) \approx \left(\frac{(L + L_g) \omega_0}{|v_{s,abc}| |v_{g,abc}|} \right) p, \quad (27)$$

where p denotes the power injected by the converter. Further, assuming regulated ac voltages, i.e., constant $|v_{s,abc}|$ and $|v_{g,abc}|$, (27) is simplified to

$$\delta \approx \alpha p \quad \text{where} \quad \alpha = \frac{(L + L_g) \omega_0}{|v_{s,abc}| |v_{g,abc}|} \quad \text{is constant.} \quad (28)$$

A similar approximation as in (28) relates δ_r to the power reference p_r . Thus, the HAC in (6) is approximated by

$$\omega \approx \omega_0 + \kappa_{dc}(v_{dc} - v_{dc,r}) - \bar{\kappa}_{ac}(p - p_r), \quad (29)$$

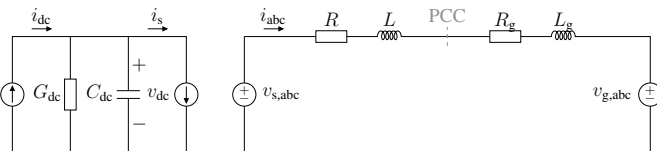


Fig. 3. The circuit diagram of the converter model connected to a weak grid model in abc-coordinates system.

where $\bar{\kappa}_{ac} = \alpha \kappa_{ac}/2$. The approximate HAC (29), can be rewritten in a trade-off form as

$$\Delta\omega \approx \kappa_{dc}\Delta v_{dc} - \bar{\kappa}_{ac}\Delta p, \quad (30)$$

where the converter frequency deviation from the nominal frequency is proportional to the dc voltage and ac power deviations from their respective references. We remark that if the assumptions behind (29) hold, the local (i.e., small-signal) stability properties of the original and approximate HAC forms are identical. Finally, note that the approximate HAC (30) coincides with the dual-port GFM control [22].

C. LC filter consideration and cascaded controllers

It is possible to consider LC output filter element which results in the model configuration in Figure 4. In this case, one can combine (29) with standard PI-based cascaded voltage and current controls [5], [7], [37]. Such control architecture is shown in Figure 5 and is briefly described as it follows.

- The phase angle defined by HAC and a prescribed reference ac voltage magnitude are combined to define the reference PCC voltage in dq-coordinates, i.e., $v_{dq,r}$. Note that the converter frequency and angle defined by integrating (29) serves as the reference angle for subsequent controllers implemented in dq0-coordinates.
- The PI-based ac voltage control (with feedforward terms) [5] processes the reference given by the GFM layer and PCC voltage feedback to define the reference filter current, i.e., $i_{dq,r}$.
- The PI-based ac current control (with feedforward terms) processes the reference given by the voltage control layer and filter current feedback to define the converter voltage to appear behind the LC filter, i.e., $v_{s,dq,r}$.
- The reference voltage given by the current control is processed by the modulation algorithm that defines m_{abc} .

We refer the reader to [5], [7], [37] for further details on the structure and tuning of such cascaded control architectures.

D. Control variants and extensions

On the basis of the GFM HAC, one can construct a few control variants. Let us introduce three different variants.

1) *Fully multi-variable variant*: the key idea behind the HAC is to include a dc feedback controller into the converter angle dynamics. Along the same direction, one can include an ac feedback controller into the converter dc dynamics. In

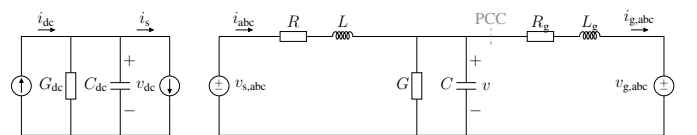


Fig. 4. The circuit diagram of the converter model with LC output filter connected to a weak grid model in abc-coordinates system; this model also represents the case of a LCL filter consideration in which the grid-side filter inductance is merged with the grid impedance.

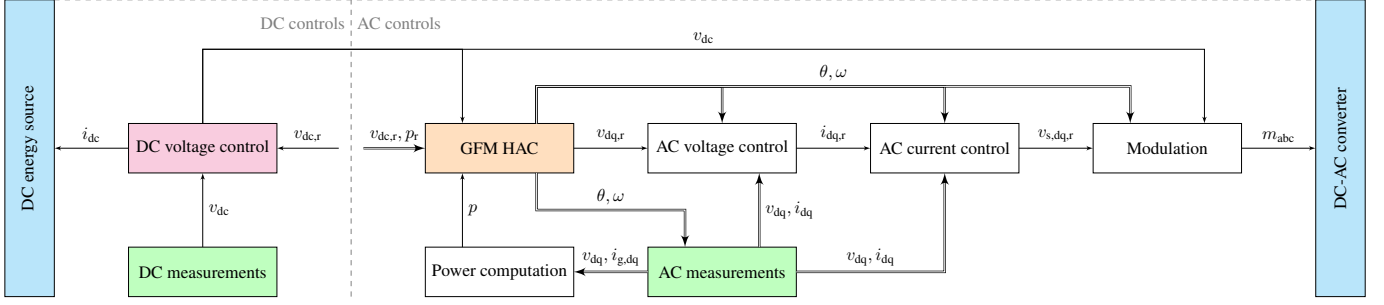


Fig. 5. The overall control architecture of a grid-connected converter system including the dc-side controls, ac-side GFM, voltage, and current controls.

a generic form, the closed-loop dynamics under such fully multi-variable control design takes the form

$$\begin{aligned} \frac{dx_{dc}}{dt} &= f_{dc}(x_{dc}, x_{ac}) + \kappa_{dc} g_{11}(x_{dc}) + \kappa_{ac \rightarrow dc} g_{12}(x_{ac}), \\ \frac{dx_{ac}}{dt} &= f_{ac}(x_{dc}, x_{ac}) + \kappa_{dc \rightarrow ac} g_{21}(x_{dc}) + \kappa_{ac} g_{22}(x_{ac}), \end{aligned}$$

where x_{dc} denotes the dc states, $f_{dc}(x_{dc}, x_{ac})$ describes the physical dc subsystem, κ_{dc} is the dc control gain, $g_{11}(x_{dc})$ is the linear/nonlinear dc controller for the dc states, $\kappa_{ac \rightarrow dc}$ is the gain of ac \rightarrow dc linear/nonlinear coupling control $g_{12}(x_{ac})$. Similarly, the states, physical ac subsystem, coupling controller gain and function, the ac control gain and function of the ac subsystem are respectively denoted by x_{ac} , $f_{ac}(x_{dc}, x_{ac})$, $\kappa_{dc \rightarrow ac}$, $g_{21}(x_{dc})$, κ_{ac} , and $g_{22}(x_{ac})$. Such augmentation of the standard GFM HAC is explored in [36].

2) *Inverse tangent variant*: one can replace the ac synchronization term in (6) by an inverse tangent function, i.e., $\tan^{-1}(\delta - \delta_r)$. Furthermore, one can consider the combination of controls in [11] with [15] to arrive at the hybrid form:

$$\omega = \omega_0 + \kappa_{dc}(v_{dc} - v_{dc,r}) - \kappa_{ac,1} \tan^{-1}(\kappa_{ac,2}(p - p_r)).$$

Note that it is possible to derive strong large-signal (i.e., global) stability guarantees for this control variant as in [20], [36]. Further, [11] highlights the improved dynamic performance of the arctan droop control in contrast to the standard droop control. Thus, one can expect similar improvements for the hybrid arctan variant versus the standard HAC.

3) *Energy-like variant*: finally, one can replace the linear dc term in (6) with a nonlinear quadratic term, i.e., $(v_{dc} - v_{dc,r})^2$ that is related to the dc energy and its reference. This control variant is particularly interesting for the modular multilevel converter (MMC) applications.

We remark that our preliminary investigations, e.g., [36], suggest that the aforementioned variants exhibit improved performance and/or lead to more relaxed conditions over the standard HAC, however, a deeper investigation is required.

V. EXPERIMENTAL VERIFICATION

In this section, we describe the employed C-HiL verification approach, and present our test results.

A. Controller-hardware-in-the-loop verification approach

To verify the proposed GFM HAC strategy under real-world effects such as discretization, delays, measurement noise, etc., we go beyond offline simulations as in [20], [25]–[27] and implement our control algorithm in a control card, in order to run C-HiL simulations. The C-HiL approach represents a good candidate in terms of balancing testing complexity, costs, and fidelity. This setup enables a high degree of automation, thereby facilitating a high coverage of cases and grid conditions, especially those hard to implement in a laboratory setup or in the field.

The utilized hardware benchmark is depicted in Figure 6, consisting of an Opal-RT OP5700 as real-time simulator, a host PC, and several Texas Instrument (LaunchPad F28379D) control cards in charge of executing the controller. The control cards receive the dc voltage and ac voltage and current as analog signals from Opal-RT, and generate the PWM signals to be sent back to the real-time simulator as digital signals. Switching frequency for the inverter is set to 5kHz, which is the same rate as for the execution of the controller in the control card. The grid-connected converter model and the dc source controller are executed in Opal-RT, using Time-Stamped Bridges to model the inverter IGBTs [38].

The testbed architecture is represented in Figure 7. The host PC communicates with the control cards via UART, and with Opal-RT via TCP/IP, thanks to the RT-LAB API. Given that the control cards possess two cores, data recording occurs in an online manner, bypassing memory limitations in the control card. Our setup allows us to measure relevant internal signals from the controllers such as frequency and filtered ac power. By means of configuration files, the tests of interest, set-points, and models to be used are defined. The tests are completely automatized, including the flashing of the control cards, building the grid models for the Opal-RT, synchronization of the cards and the real-time simulator, and finally the retrieval of all data of interest.

B. C-HiL verification test scenarios

In what follows, we provide the results of four verification test cases that are performed on the testbed shown in Figure 6. Let us begin by highlighting the combination of employed controllers. We consider the PI-based dc and ac voltage control as described in Section II, and the approximate power-based implementation of the HAC presented in Section IV. The

baseline grid-connected converter model that is implemented in Opal-RT corresponds to the circuit configuration illustrated in Figure 4. Finally, the baseline model and control parameters are presented in Table I. Note that the test-specific model and parameters modifications are described case-by-case.

1) *Accuracy verification and islanded GFM operation:* in this test scenario, the grid model is removed from the configuration in Figure 4. Instead a resistive load is connected

at the PCC which at rated ac voltage consumes 0.5 p.u. active power. Figure 8 illustrates the behavior of the islanded converter under the HAC in offline and C-HiL simulations. Note that a 0.5 p.u. load increase is applied at $t = 0.1$ s. The results of offline and C-HiL simulations are sufficiently close, thus, verifying the accuracy of C-HiL testbed. Furthermore, the dynamic behavior shown in Figure 8 verifies the performances of the HAC control in islanded configuration. Note that, the ac gain (i.e., the droop gain) is selected such that it results in 5% frequency deviation for 1 p.u. active power disturbance. Observe that the 0.5 p.u. results in 2.5% frequency drop in Figure 8, thus, verifying the drooping behavior of the approximate HAC (29). Finally, the dc voltage is recovered to the reference value due to the integral term.

2) *Grid-connected GFM operation:* in this scenario, model configuration is identical to the one showed in Figure 4 and HAC behavior is investigated w.r.t. a set-point change event in grid-connected mode. Figure 9 shows that GFM HAC not only preserves synchronization with the grid under a relatively large active power set-point change, i.e., 0.5 p.u. increase, but also achieves zero post-event steady-state error and stabilizes the converter frequency at the desired reference. We remark that the difference in transient behaviors in Figures 8 and 9 originates from the natural damping influence of the resistive load in the previous test scenario. Finally, retuning the GFM control parameters and the cut-off frequency of the low-pass filter applied to ac power measurement allows to realize a first-order behavior following the set-point change event. However, for the sake of consistency the parameters are kept identical.

3) *Grid frequency variation:* in this scenario, the grid frequency is increased step-wise by 5%. Figure 10 highlights the behavior of grid-connected converter under the HAC. Note that the GFM HAC preserves system stability w.r.t. a relatively severe contingency. This is underpinned by the large-signal (i.e., global) stability of the HAC established in [20]. Further, due to the particular choice of the droop gain, the converter active power injection drops by 1 p.u. and reverses the power flow to provide frequency support.

4) *Two-converter load-sharing operation:* finally, we consider a two-converter test scenarios. In this case, the converter models correspond to the model shown in Figure 4. However, the grid model is removed and the converters are connected through two RL line models and a resistive load is connected in the middle. Note that the droop gains for the power converters are slightly different, i.e., $0.98\bar{\kappa}_{ac}$ and $1.02\bar{\kappa}_{ac}$. Figure 11 illustrates the behavior of the system when a load increase event is applied. Observe that the post-disturbance frequency synchronization is achieved while the converters exhibits slightly different load-sharing according to the prescribed droop gains.

VI. CONCLUSION

In this work, we discussed the behavioral properties of the GFM HAC, described required complementary controls, provided a closed-loop analysis involving analytical operating point evaluation and energy-based nonlinear stability analysis, derived an approximation of the HAC, and introduced several

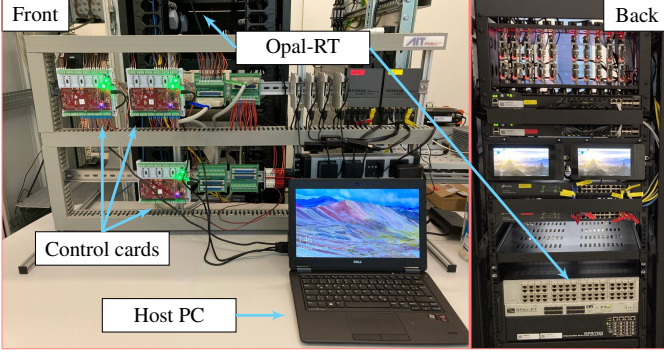


Fig. 6. C-HiL testbed that includes three external control cards connected to Opal-RT OP5700. The host PC is used to automatically run C-HiL simulations and collect the results.

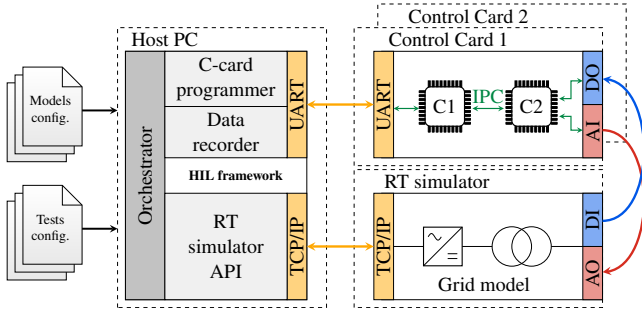


Fig. 7. C-HiL testbed architecture. The C-HiL framework (on the left side) is developed in Python and its main functionality is to coordinate the RT-simulator and control cards. The control cards (on the right side) are connected to the RT-simulator via physical cables.

TABLE I
GRID-CONNECTED CONVERTER MODEL AND CONTROL PARAMETERS.

Symbol	Description	Value
p_b	base power	500 kVA
f_b	base frequency	60 Hz
ω_0	reference angular frequency	$2\pi f_b$
v_0	reference grid voltage magnitude	326.59 V
$v_{dc,r}$	reference dc-link voltage	$3v_0$
G_{dc}	dc-side conductance	$0.01 \text{ m}\Omega^{-1}$
C_{dc}	dc-link capacitance	0.01 F
f_{sw}	switching frequency	5 kHz
L	ac filter inductance	0.12 mH
C	ac filter capacitance	0.13 mF
L_g	grid equivalent inductance	0.56 mH
R_g	grid equivalent resistance	0.064Ω
κ_p	dc voltage control proportional gain	10
κ_i	dc voltage control integral gain	500
$\kappa_{p,ac}$	PCC voltage control proportional gain	0.1
$\kappa_{i,ac}$	PCC voltage control integral gain	20
κ_{dc}	HAC dc gain	0.18
$\bar{\kappa}_{ac}$	HAC ac gain	18.84

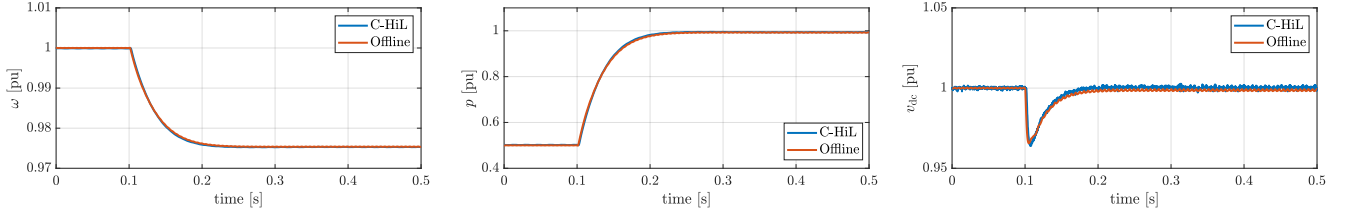


Fig. 8. The time-evolution of normalized frequency (left), active power (middle), and dc voltage (right) of an islanded GFM converter under HAC w.r.t. a load disturbance scenario in offline and C-HiL simulations.

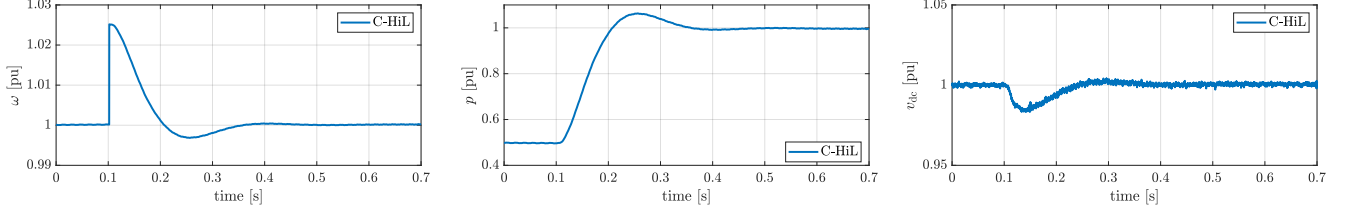


Fig. 9. The time-evolution of normalized frequency (left), active power (middle), and dc voltage (right) of a grid-connected GFM converter under HAC w.r.t. a power set-point change scenario in C-HiL simulations.

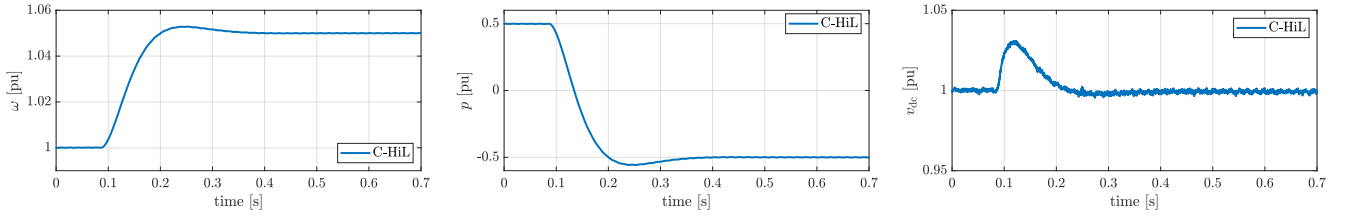


Fig. 10. The time-evolution of normalized frequency (left), active power (middle), and dc voltage (right) of a grid-connected GFM converter under HAC w.r.t. a grid frequency variation scenario in C-HiL simulations.

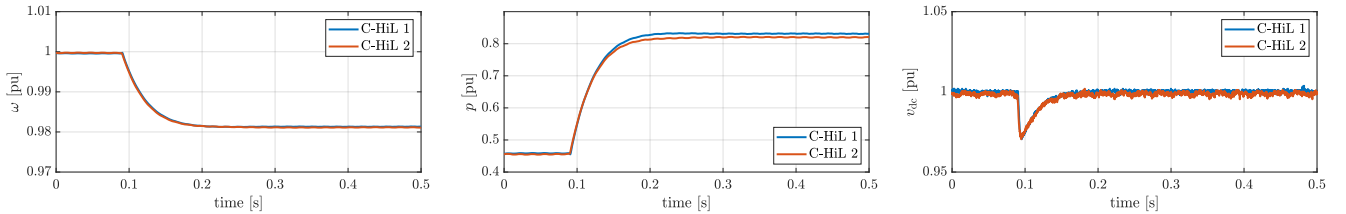


Fig. 11. The time-evolution of normalized frequency (left), active power (middle), and dc voltage (right) of two coupled GFM converters under HAC (with slightly different droop gains) w.r.t. a load disturbance scenario in C-HiL simulations.

extensions of the standard HAC. Last but not least, the control performance was verified by several C-HiL test scenarios. Our agenda of future work includes the stability analysis and performance verification of the HAC variants, and power hardware validation of the control concept.

REFERENCES

- [1] N. Hatziaargyriou, J. Milanovic, C. Rahmann, V. Ajjarapu, C. Canizares, I. Erlich, D. Hill, I. Hiskens, I. Kamwa, B. Pal *et al.*, “Definition and classification of power system stability—revisited & extended,” vol. 36, no. 4, pp. 3271–3281, 2020.
- [2] Y. Lin, J. H. Eto, B. B. Johnson, J. D. Flicker, R. H. Lasseter, H. N. Villegas Pico, G.-S. Seo, B. J. Pierre, and A. Ellis, “Research roadmap on grid-forming inverters,” National Renewable Energy Lab. (NREL), Tech. Rep., 2020.
- [3] A. Crivellaro, A. Tayyebi, C. Gavriluta, D. Groß, A. Anta, F. Kupzog, and F. Dörfler, “Beyond low-inertia systems: Massive integration of grid-forming power converters in transmission grids,” in *IEEE Power & Energy Society General Meeting (PESGM)*, 2020, pp. 1–5.
- [4] F. Milano, F. Dörfler, G. Hug, D. J. Hill, and G. Verbič, “Foundations and challenges of low-inertia systems,” in *power systems computation conference (PSCC)*, 2018.
- [5] A. Tayyebi, D. Groß, A. Anta, F. Kupzog, and F. Dörfler, “Frequency stability of synchronous machines and grid-forming power converters,” *IEEE Trans. Emerg. Sel. Topics Power Electron.*, vol. 8, no. 2, pp. 1004–1018, 2020.
- [6] J. Rocabert, A. Luna, F. Blaabjerg, and P. Rodríguez, “Control of power converters in ac microgrids,” *IEEE Trans. Power Electron.*, vol. 27, no. 11, pp. 4734–4749, 2012.
- [7] U. Markovic, O. Stanojevic, P. Aristidou, E. Vrettos, D. Callaway, and G. Hug, “Understanding small-signal stability of low-inertia systems,” vol. 36, no. 5, pp. 3997–4017, 2021.
- [8] “Great Britain grid forming best practice guide,” National Grid ESO, Tech. Rep., 2023.
- [9] “Engineering roadmap to 100% renewables,” Australian Energy Market Operator (AEMO), Tech. Rep., 2022.
- [10] M. Chandorkar, D. Divan, and R. Adapa, “Control of parallel connected inverters in standalone AC supply systems,” *IEEE Trans. Ind. Appl.*, vol. 29, no. 1, pp. 136–143, 1993.
- [11] C. N. Rowe, T. J. Summers, R. E. Betz, D. J. Cornforth, and T. G. Moore, “Arctan power–frequency droop for improved microgrid stability,” *IEEE*

- Trans. Power Electron.*, vol. 28, no. 8, pp. 3747–3759, 2012.
- [12] H. Yu, M. Awal, H. Tu, I. Husain, and S. Lukic, “Comparative transient stability assessment of droop and dispatchable virtual oscillator controlled grid-connected inverters,” *IEEE Trans. Power Electron.*, vol. 36, no. 2, pp. 2119–2130, 2021.
 - [13] Q. C. Zhong and G. Weiss, “Synchronverters: inverters that mimic synchronous generators,” *IEEE Trans. Ind. Electron.*, vol. 58, no. 4, pp. 1259–1267, 2011.
 - [14] M. Chen, D. Zhou, and F. Blaabjerg, “Enhanced transient angle stability control of grid-forming converter based on virtual synchronous generator,” *IEEE Trans. Ind. Electron.*, vol. 69, no. 9, pp. 9133–9144, 2021.
 - [15] C. Arghir and F. Dörfler, “The electronic realization of synchronous machines: Model matching, angle tracking, and energy shaping techniques,” *IEEE Trans. Power Electron.*, vol. 35, no. 4, pp. 4398–4410, 2019.
 - [16] I. Cvetkovic, D. Boroyevich, R. Burgos, C. Li, and P. Mattavelli, “Modeling and control of grid-connected voltage-source converters emulating isotropic and anisotropic synchronous machines,” in *IEEE Workshop on Control and Modeling for Power Electronics (COMPEL)*, 2015.
 - [17] S. A. Aghdam and M. Agamy, “Virtual oscillator-based methods for grid-forming inverter control: A review,” *IET Renew. Power Gener.*, vol. 16, no. 5, pp. 835–855, 2022.
 - [18] G.-S. Seo, M. Colombino, I. Subotic, B. Johnson, D. Groß, and F. Dörfler, “Dispatchable virtual oscillator control for decentralized inverter-dominated power systems: Analysis and experiments,” in *IEEE Applied Power Electronics Conference and Exposition (APEC)*, 2019.
 - [19] M. Awal, M. R. K. Rachi, H. Yu, I. Husain, and S. Lukic, “Double synchronous unified virtual oscillator control for asymmetrical fault ride-through in grid-forming voltage source converters,” *IEEE Trans. Power Electron.*, 2022.
 - [20] A. Tayyebi, A. Anta, and F. Dörfler, “Grid-forming hybrid angle control and almost global stability of the dc-ac power converter,” *IEEE Transactions on Automatic Control*, 2022.
 - [21] Y. Gao, H.-P. Ren, and J. Li, “Grid-forming converters control based on dc voltage feedback,” 2020, Preprint available at <https://arxiv.org/abs/2009.05759>.
 - [22] D. Groß, E. Sánchez-Sánchez, E. Prieto-Araujo, and O. Gomis-Bellmunt, “Dual-port grid-forming control of mmcs and its applications to grids of grids,” *IEEE Transactions on Power Delivery*, vol. 37, no. 6, pp. 4721–4735, 2022.
 - [23] M. Chen, D. Zhou, A. Tayyebi, E. Prieto-Araujo, F. Dörfler, and F. Blaabjerg, “Generalized multivariable grid-forming control design for power converters,” *IEEE Trans. Smart Grid*, vol. 13, no. 4, pp. 2873–2885, 2022.
 - [24] J. W. Simpson-Porco, F. Dörfler, and F. Bullo, “Synchronization and power sharing for droop-controlled inverters in islanded microgrids,” *Automatica*, vol. 49, no. 9, pp. 2603–2611, 2013.
 - [25] A. Tayyebi and F. Dörfler, “Hybrid angle control and almost global stability of non-synchronous hybrid ac/dc power grids,” in *IEEE Conference on Decision and Control (CDC)*, 2022.
 - [26] A. Tayyebi, A. Anta, and F. Dörfler, “Almost globally stable grid-forming hybrid angle control,” in *IEEE Conference on Decision and Control (CDC)*, 2020.
 - [27] A. Tayyebi, A. Magdaleno, D. Vettoretti, M. Chen, E. Prieto-Araujo, A. Anta, and F. Dörfler, “System-level performance and robustness of the grid-forming hybrid angle control,” *Electric Power Systems Research*, vol. 212, p. 108503, 2022.
 - [28] C. Arghir, T. Jouini, and F. Dörfler, “Grid-forming control for power converters based on matching of synchronous machines,” *Automatica*, vol. 95, pp. 273–282, 2018.
 - [29] A. Yazdani and R. Iravani, *Voltage-sourced converters in power systems: modeling, control, and applications*. John Wiley & Sons, 2010.
 - [30] G. E. Colón-Reyes, K. C. Stocking, D. S. Callaway, and C. J. Tomlin, “Stability and robustness of a hybrid control law for the half-bridge inverter,” 2022, preprint available at: <https://arxiv.org/abs/2204.07539>.
 - [31] C. Albea, O. L. Santos, D. Z. Prada, F. Gordillo, and G. Garcia, “Hybrid control scheme for a half-bridge inverter,” *IFAC-PapersOnLine*, vol. 50, no. 1, pp. 9336–9341, 2017.
 - [32] S. Curi, D. Groß, and F. Dörfler, “Control of low-inertia power grids: a model reduction approach,” in *IEEE Conference on Decision and Control (CDC)*, 2017.
 - [33] S. Samanta, N. R. Chaudhuri, and C. Lagoa, “Fast frequency support from grid-forming converters under dc-and ac-side current limits,” *IEEE Transactions on Power Systems*, 2022.
 - [34] S. Samanta and N. R. Chaudhuri, “Stability analysis of grid-forming converters under dc-side current limitation in primary frequency response regime,” *IEEE Transactions on Power Systems*, vol. 37, no. 4, pp. 3077–3091, 2021.
 - [35] A. Ulbig, T. S. Borsche, and G. Andersson, “Impact of low rotational inertia on power system stability and operation,” in *IFAC Proceedings Volumes*, 2014.
 - [36] A. Gattiglio, “Multi-variable arctan hybrid angle control and global stability of grid-forming power converters,” 2021, Thesis available at: <http://dx.doi.org/10.13140/RG.2.2.18935.75684>.
 - [37] I. Subotić, D. Groß, M. Colombino, and F. Dörfler, “A Lyapunov framework for nested dynamical systems on multiple time scales with application to converter-based power systems,” *IEEE Trans. Autom. Control*, vol. 66, no. 12, pp. 5909–5924, 2020.
 - [38] C. Dufour and J. Bélanger, “Real-time simulation of a 48-pulse GTO STATCOM compensated power system on a Dual-Xeon PC using RTLAB,” in *International Conference on Power Systems Transients*, 2005.